# Journal of Materials Chemistry A



**PAPER** 

View Article Online
View Journal



Cite this: DOI: 10.1039/d1ta10944h

# Light-ferroelectric interaction in two-dimensional lead iodide perovskites†

Dohyung Kim, <sup>©</sup> <sup>a</sup> Anton V. Ievlev, <sup>©</sup> <sup>b</sup> Olga S. Ovchinnikova, <sup>c</sup> Sergei V. Kalinin and Mahshid Ahmadi <sup>©</sup> \*

The unique physical properties of two-dimensional (2D) metal halide perovskites (MHPs) such as nonlinear optics, anisotropic charge transport, and ferroelectricity have made these materials promising candidates for multifunctional applications. Recently, fluorine derivatives such as 4,4-difluoropiperidinium lead iodide perovskite or (4,4-DFPD, C<sub>5</sub>H<sub>10</sub>F<sub>2</sub>N)<sub>2</sub>PbI<sub>4</sub> have shown strong ferroelectricity as compared to other 2D MHPs. Although it was previously addressed that the ferroelectricity in MHPs can be affected by illumination, the underlying physical mechanisms of light-ferroelectricity interaction in 2D MHPs are still lacking. Here, we explore the electromechanical responses in 4,4-(DFPD)₂PbI₄ thin films using advanced scanning probe microscopy techniques revealing ferroelectric domain structures. Hysteretic ferroelectric loops measured by contact-Kelvin probe force microscopy are dependent on domain structures under dark conditions, while ferroelectricity weakens under illumination. The X-ray diffraction patterns exhibit significant changes in preferential orientation of individual lattice planes under illumination. Particularly, the reduced intensity of the (1 1 1) lattice plane under illumination leads to transitioning from a ferroelectric to a paraelectric phase. The instability of positive ions, especially molecular organic cations, is observed under illumination by time-of-flight secondary ion mass spectrometry. The combination of crystallographic orientation and chemical changes under illumination clearly contributes to the origin of light-ferroelectricity interaction in 2D (4,4-DFPD, C<sub>5</sub>H<sub>10</sub>F<sub>2</sub>N)<sub>2</sub>PbI<sub>4</sub>.

Received 24th December 2021 Accepted 26th March 2022

DOI: 10.1039/d1ta10944h

rsc.li/materials-a

# Introduction

Metal halide perovskites (MHPs) have gained much attention from the scientific community due to their easy and inexpensive fabrication method and their outstanding optoelectronic properties. As compared to the three-dimensional (3D) structure, 2D layered MHPs have a greater structural diversity due to breaking the tolerance space of the 3D framework. AD MHPs have shown higher ambient stability resulting from a strong interlocking force between the organic and inorganic species. In addition, this class of perovskites has shown unique physical characteristics such as optical nonlinearity, anisotropic charge carrier transport, large exciton binding energy, and ferroelectricity. Thus, 2D MHPs can be promising candidates for many optoelectronic functionalities.

Typically, ferroelectricity *i.e.* the switchable polarization with long-range ordered domains and hysteretic behavior is suitable for applications in nonlinear optical applications, nonvolatile memory, and energy storage devices. Recently, ferroelectricity has been frequently observed in a number of 2D MHPs. 11-19 The 2D MHP ferroelectrics have a general chemical formula of A<sub>2</sub>BX<sub>4</sub> where large organic cations are placed between the inorganic layers (BX<sub>4</sub>). This structure allows 2D MHPs to have multiple quantum wells, in addition to the large freedom of organic cation motions which lead to ferroelectricity in these materials.

The one effective strategy for higher spontaneous polarization ( $P_{\rm s}$ ) in 2D MHP ferroelectrics is to design A-site cations by substitution of hydrogen with fluorine.<sup>20,21</sup> The fluorine substitution as the most electronegative element, with a van der Waals radius of around 147 pm which is similar to that of the hydrogen atom (120 pm) can have a minor structural distortion for tuning the physical properties, *e.g.*, the polarization state. This can be found in recently developed 2D MHPs showing stronger ferroelectricity.<sup>22,23</sup> Most recently, 4,4-difluoropiperidinium (DFPD) that includes fluorine derivatives was introduced into PbI<sub>4</sub> octahedral layers, resulting in higher  $P_{\rm s} \sim 10~\mu C$  cm<sup>-2</sup> at room temperature.<sup>17</sup> This 2D composition possesses relatively larger spontaneous polarization as compared to other molecular ferroelectrics.<sup>9</sup> Our recent study demonstrated that ferroelectricity can be only observed in the low strain (4,4-

<sup>&</sup>lt;sup>a</sup>Institute for Advanced Materials and Manufacturing, Department of Materials Science and Engineering, University of Tennessee, Knoxville, TN 37996, USA. E-mail: mahmadi3@utk.edu

<sup>&</sup>lt;sup>b</sup>Center for Nanophase Materials Sciences, Oak Ridge National Laboratory, Oak Ridge, TN 37830, USA

<sup>\*</sup>Computational Science and Engineering Division, Oak Ridge National Laboratory, Oak Ridge, TN 37830, USA

<sup>†</sup> Electronic supplementary information (ESI) available. See DOI: 10.1039/d1ta10944h

 $\mathrm{DFPD})_2\mathrm{PbI}_4$  thin films.<sup>24</sup> Nevertheless, further efforts to elucidate underlying mechanisms behind ferroelectricity are necessary for this material.

Particularly, the interplay of light and ferroelectricity, the socalled photo-ferroelectricity, is an important scientific question as ferroelectricity in MHPs remains an academic curiosity. The light-ferroelectricity interaction including bulk and depolarization field-driven photovoltaic effects, domain wall motions, and the Schottky barrier effect, has been extensively studied in classical ferroelectrics and 3D MHPs.25 Despite numerous efforts, the interplay of light and ferroelectricity is unexplored in 2D MHPs. It is well known that the ferroelectricity in 2D MHPs stems from the dipole moment of organic cations. Ferroelectricity has been experimentally demonstrated using various characterization tools. However, the potential possibilities such as chemical dynamics and crystallographic orientations, directly correlating with ferroelectricity have not been studied yet. In fact, the interplay between surface-charged ions and bulk spontaneous polarization can lead to mixed states in ferroelectric films.26 Unlike classical ferroelectrics, highly ordered ionic states in MHPs provide an electrochemically driven polarization, which has led to ferroelectric-like behavior in 3D polycrystalline perovskite films.<sup>27</sup> Even though the mobile ions in 2D MHPs are tightly locked as compared to 3D counterparts, ion migration still exists in 2D MHPs,28 thus it is essential to explore the origin of ferroelectricity in materials with ion dynamics. Another important implication is crystallographic orientation. It has been well established that crystallographic orientations in MHPs have an impact on optoelectronic properties such as surface photovoltage, charge transport, and charge carrier recombination.29-31 Our recent studies discuss the correlation between crystallographic orientations and ferroelastic twin domains in 3D MHPs.32 This study reveals that different crystallographic orientations between adjacent twin domains contribute to non-ferroelectricity.32 The intrinsic properties of 2D MHPs could possibly change under illumination leading to interesting phenomena<sup>33-35</sup> as observed in 3D MHPs. These have motivated us to explore the light induced ferroelectricity changes in 2D (4,4-DFPD)<sub>2</sub>PbI<sub>4</sub>.

In this study, (4,4-DFPD)<sub>2</sub>PbI<sub>4</sub> crystals are successfully grown by a slow cooling crystallization method, and then thin films are fabricated by drop-casting from the as-grown crystals dissolved in dimethyl sulfoxide. Details of crystal growth and film fabrication can be found in our previous work.24 We explore the electromechanical responses on the film surface using band excitation piezo-response force microscopy (BE-PFM). Further, contact Kelvin probe force microscopy (cKPFM), an advanced piezo-response force microscopy (PFM) technique, detects the electromechanical responses using a first-order reversal curve (FORC) electrical waveform that is composed of gradually increasing and decreasing stepwise electrical biases. To investigate the light effect, we perform cKPFM measurements under illumination after the measurement in the dark. X-ray diffraction (XRD) is carried out to study crystallographic orientations under external stimuli such as illumination and electric bias. Time-of-flight secondary ion mass spectrometry (ToF-SIMS) is performed to demonstrate the chemical dynamics of the film

surface in the dark and under light conditions. Our results elucidate the origin of the light–ferroelectric interaction in  $(4,4-DFPD)_2PbI_4$  thin films.

## Results & discussion

Our previous study demonstrated that only (4,4-DFPD)<sub>2</sub>PbI<sub>4</sub> thin films fabricated by drop-casting lead to superior ferroelectricity.<sup>24</sup> To investigate the electromechanical responses and ferroelectricity on the film surface, scanning probe microscopy (SPM) including atomic force microscopy (AFM), PFM, BE-PFM, and cKPFM measurements were performed in dark and under illumination using an Asylum Research AFM (MFP-3D) with a Labview/National Instruments setup. BE measurements *e.g.*, BE-PFM and cKPFM were carried out by tracking the contact resonance frequency in the BE mode. Note that all measurements were taken under ambient air conditions in a low relative humidity below 20%. We note that the samples were stable and did not show any topological changes during repetitive scans in the same areas.

Fig. 1 shows the corresponding topography, BE-PFM amplitude, and phase in (4,4-DFPD)<sub>2</sub>PbI<sub>4</sub> thin films in dark and under illumination. Other BE-PFM frequency and quality factor (Q) maps are displayed in Fig. S1.† The selected scan areas in Fig. 1 are chosen from the larger scans (see Fig. S2†), revealing ferroelectric domains in the phase maps. In the dark, the observed electromechanical amplitude responses (Fig. 1b) are almost similar as compared to the responses under illumination (Fig. 1e). To compare the amplitude responses between the two conditions, histogram plots are shown in Fig. S3<sup>†</sup>, and additional information including the results of a standard ferroelectric sample is described in ESI Note 1.† As previously shown by us,24 ferroelectric domains are observed by the phase flips of 180° in both phase maps (Fig. 1c and f). However, academic curiosity still remains regarding the observed ferroelectric domains' properties and their origin in 2D MHPs which can be further studied. Nonetheless, the alternating domain structures are clearly visible in similar locations both in the dark and under illumination. Note that the ferroelectric domains in (4,4-DFPD)<sub>2</sub>PbI<sub>4</sub> thin films were confirmed via BE-PFM by us24 and classical PFM by others.17

PFM techniques have limited insight into electromechanical responses especially when the film surfaces are not smooth since the larger topological changes can typically lead to measurement artifacts. Thus, we utilize the cKPFM technique as an advanced PFM mode, exploring both electromechanical and electrostatic phenomena using a complex electrical pulsed bias waveform.  $^{36,37}$  In cKPFM spectroscopy, gradual stepwise pulsed biases with the on- and off-field, the so-called first order reversal curve (FORC) (see Fig. 2a), applies to a conductive AFM tip where the biases are denoted as  $V_{\rm write}$  and  $V_{\rm read}$ . The  $V_{\rm write}$  (DC pulse) is used to change the functional response, e.g., the surface potential or ferroelectric switching while the  $V_{\rm read}$  as a subsequent small DC voltage tracks changes in electrostatic forces.

As discussed, we perform cKPFM measurements in similar regions in the dark and under illumination. Fig. 2 shows

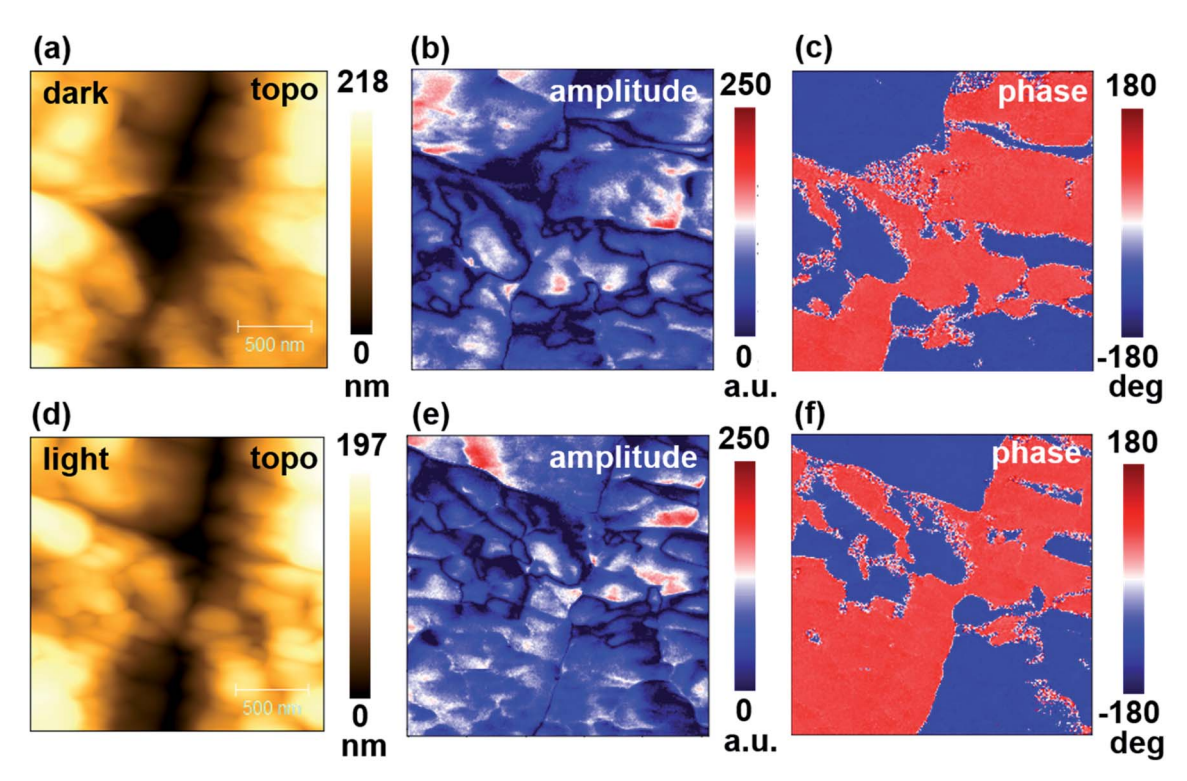


Fig. 1 BE-PFM images of the (4,4-DFPD)<sub>2</sub>Pbl<sub>4</sub> thin film in the dark (top row) and under illumination (bottom row). The full scan size is over an area of 2  $\mu$ m<sup>2</sup>. (a) Topography, (b) BE-PFM amplitude, and (c) phase in the dark and (d-f) under illumination.

averaged cKPFM responses from all 1600 pixels over an area of 2  $\mu$ m<sup>2</sup> as a function of biases, ranging from -10 V to +10 V. Here, the duration of the bias steps is around 16 milliseconds (ms). The choice of the 16 ms time step is limited by the bandwidth of the cKPFM measurements. This method utilizes a complex waveform composed of multiple hysteresis loops per spatial pixel. Given the limitation of 1-10 s per spatial pixel, the duration of the single-bias step cannot exceed 10-20 ms. At the same time, given the relatively weak PFM signal in this material where cKPFM responses are basically from the multiplication of PFM amplitude and phase responses, smaller bias times result in unacceptably low signal-to-noise ratios. The used millisecond pulse duration in cKPFM measurements allows exploring ferroelectricity. Specifically, this time scale with on- and off-field leads to injection and relaxation of charge carriers, and then

polarized charge states (ferroelectric responses) are measured under off-field conditions. The millisecond time scale under dark conditions could activate electronic charge carriers in MHPs and charge injection, rather than ion migration that occurs within either sub- or several seconds or minute time scale as demonstrated in many studies.38-43 However, at high biases, the applied pulse duration could also drive ion migration. Therefore, during our measurements, it is expected that both electronic and ionic charge carriers transit in 2D MHPs. However, this phenomenon is less effective than in 3D MHPs due to suppressed ionic motions in 2D MHPs44 in that there is a strong interlocking force between the organic and inorganic sublattice. Note that the spectroscopic experiments were performed consecutively from top-left to right, moved to the next line, and then down to the 40<sup>th</sup> line in the same way in the dark

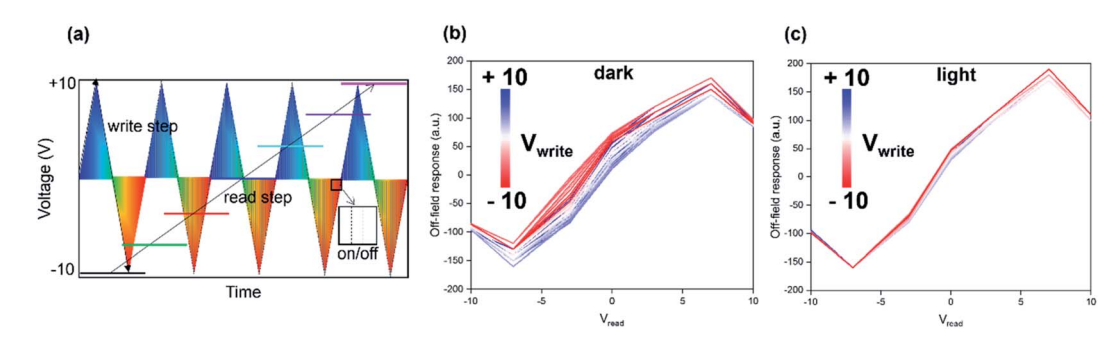


Fig. 2 (a) Schematic illustration of the FORC electrical bias waveform in cKPFM measurements. Averaged cKPFM curves on a  $40 \times 40$  grid with a  $2 \times 2$   $\mu$ m area upon application of different pulsed bias voltages (b) in the dark and (c) under illumination.

and then under illumination. During the measurements under illumination, the scanned location was slightly shifted (a few micrometers) due to thermal drift as the measurements take over 17 hours but both locations in the dark and under illumination are within one large crystal (Fig. S2c†). Besides, we cannot observe any topological change after both measurements. Thus, we believe that our results are not directly correlated with the damaged film surface. Nonetheless, we cannot completely rule out the internal changes by photogenerated charge carriers in the bulk films during the measurements. To verify if this phenomenon is due to accumulated bias steps, we perform two consecutive cKPFM measurements on the same location in the dark. Despite slightly different responses, similar results are revealed as shown in Fig. S4.† Thus, it is apparent that the cKPFM response with narrow bands in Fig. 2c results from illuminating the film surface.

As described above, it is interesting to note that the band dispersions in the cKPFM curves are significantly different under dark and light conditions in Fig. 2b and c. We previously observed hysteretic responses at some specific locations in the same material,24 which were also offset by many non-hysteretic responses. Consequently, in the averaged cKPFM responses, hysteretic behavior can be significantly reduced. Similarly, in the current study, the hysteretic behavior is significantly decreased under both conditions due to either less hysteretic or non-hysteretic responses at more pixels. Particularly, while larger band dispersion is observed in the dark, the cKPFM response is narrow and almost linear under illumination. In Fig. 2b and c, the cKPFM data are from the averaged curves of all pixels. As a result, band dispersion depends on the number of data points with lower band dispersion. According to our previous studies,45,46 larger band dispersion is induced under illumination in 3D MHPs due to the higher density of charge carriers. In fact, the linear curve in the cKPFM responses is associated with pure electrostatic behavior and transition to paraelectricity while the larger band dispersion is induced by a higher density of charge carriers including photogenerated charge carriers and mobile ion species. Nonetheless, our results reveal the larger band dispersion only in the dark as compared to under light conditions. Therefore, we further investigate the cKPFM curves in individual pixels comparing ferroelectric domain structures in the next section.

Fig. 3a–j shows the corresponding loading map of phase responses and cKPFM curves in several representative pixels in the dark and under illumination. In the dark, the phase map in Fig. 3a shows the corresponding domain structures as shown in Fig. 1. Other responses including the amplitude, frequency, and *Q*-factor maps are displayed in Fig. S5.† We rule out the areas marked in red circles in Fig. S5b† as a significant shift of contact resonance leads to artifacts in the responses. This frequency shift originates from larger topographic variations. Interestingly, we observe strong hysteretic behaviors (Fig. 3b and c) in blue regions in the phase maps while less hysteretic behaviors (Fig. 3d and e) are observed in red regions of the phase maps. To further investigate hysteretic behaviors at more pixels, we have shown more cKPFM responses in Fig. S6 and S7.† As a result, the larger hysteresis loops in the cKPFM responses correspond

to the blue regions in the phase map while the reduced hysteresis loops are observed in the red regions on the map. Our results indicate that local hysteretic dynamics are dependent on either orientation of polarization or the domain structure. Such switchable electromechanical responses stem from various parameters such as charge injection, ion migration, and the electrochemical strain by ionic motions.<sup>47</sup> We will discuss the chemical dynamics studied by ToF-SIMS in this material in the later section.

To explore the potential role of ion dynamics, we apply FORC biases to the film surface through the conductive AFM tip which results in hysteretic behaviors in cKPFM curves during offfields. Note that it requires a higher electric field (>30 V) for complete domain switching as described by Xiong et al.17 However, it has been previously demonstrated via cKPFM that the FORC bias can allow lower switching biases (<10 V) in cKPFM curves, compared with a normal on-field bias sweep. This is due to either different film quality or accumulated bias steps during FORC biases. It is well known that the nonferroelectric effects can also lead to hysteresis in PFM that convincingly imitates the ferroelectric behavior with bistable states.47 Thus, clarifying that the ferroelectricity at the nanoscale is not confined to only PFM study. With this demand, it has been well established that cKFPM is a complementary technique allowing to distinguish between ferroelectric and non-ferroelectric materials.37 Therefore, we adopt the cKPFM technique to identify the ferroelectricity and ionic motions in 2D MHPs. Despite the ongoing controversy in 3D MHPs, ferroelectricity is consistently observed in 2D MHPs via various characterization tools such as PFM, 11,12,14-19,24 current-voltage (I-V) characteristics,  $^{11,12,15,17-19}$  the polarization-electric (P-E) loop, 11-13,15-19 permittivity, 11-15,17,19 second harmonic generation (SHG), 11-15,17-19 and cKPFM.24

Here, despite an effective ferroelectric behavior in the dark, the observed ferroelectricity is significantly reduced under illumination as shown in Fig. 3f-j. Particularly, the minor hysteretic behavior (see Fig. 3g and h) is only observed at a few pixels. The noticeable lower band dispersion under illumination in Fig. 3i and j indicates the non-ferroelectric nature of the film. In the cKPFM response, the band dispersion is a measure of the charge injection onto the film surface where larger band dispersion represents a higher density of charge carriers. 48,49 As shown in the cKPFM response under illumination, the narrow band dispersion (Fig. 3i and j) identifies the pure electrostatic nature as non-ferroelectricity. Further, the linear shape (lower band dispersion) in the cKPFM response results from transition to paraelectricity.50 Other responses including the amplitude, frequency, and Q-factor maps are displayed in Fig. S8.† Additional cKPFM curves at different pixels are shown in Fig. S9 and S10.† However, most pixels exhibit linear cKPFM curves indicating either weak or no ferroelectricity regardless of domain structures under illumination.

In our cKPFM results, band dispersion is strongly dependent on the negative and positive PFM phases under dark conditions, which corresponds to the opposite orientation of spontaneous polarization in different ferroelectric domains. We suspect that such dependence under dark conditions derives from chemical

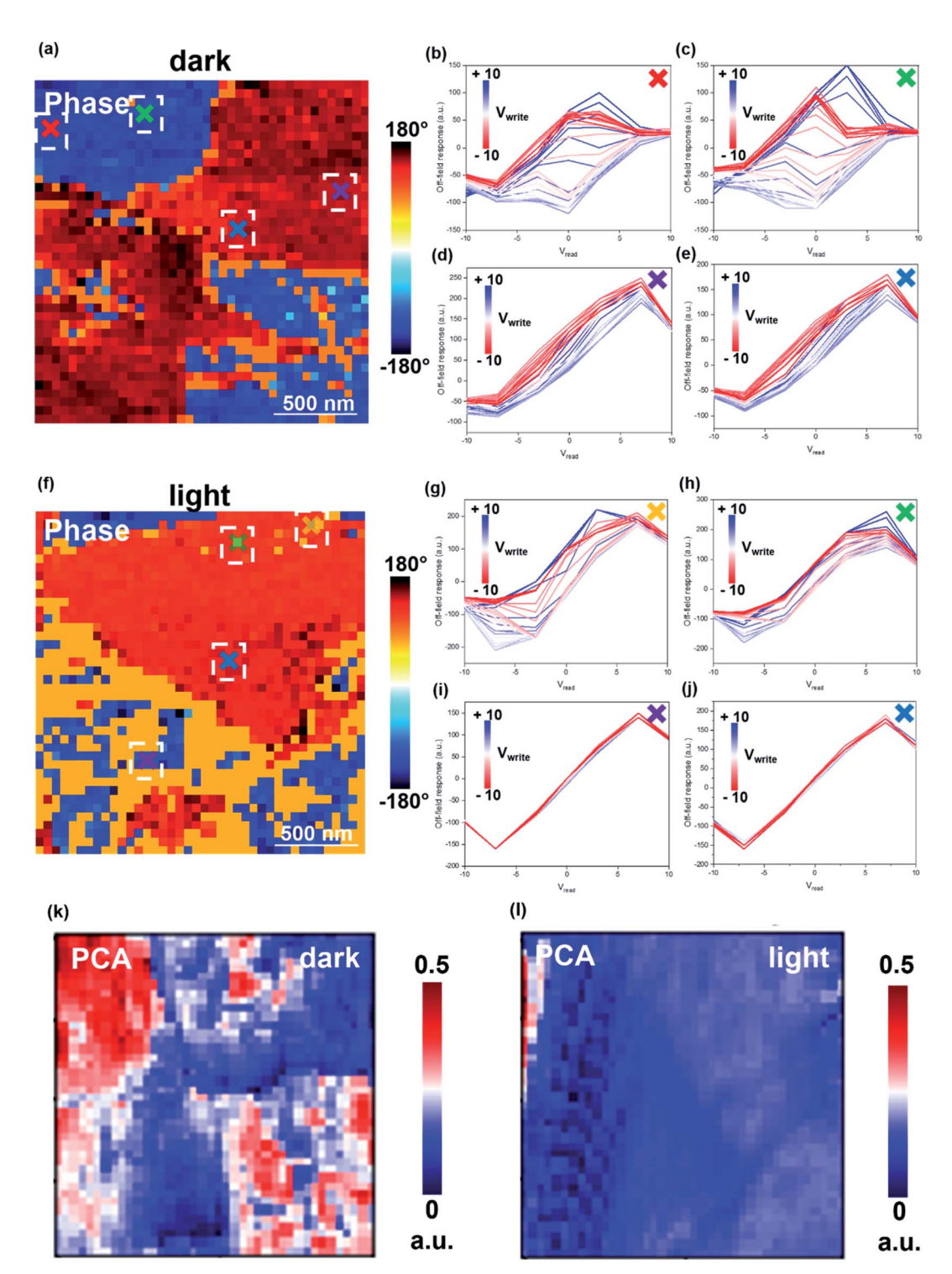


Fig. 3 (a) The loading map of phase responses in cKPFM measurements in the dark where the ferroelectric domain is observed in BE-PFM measurements. Individual cKPFM curves at the 'x' marked in (b) red, (c) green, (d) purple, and (e) light-blue in (a). (f) The loading map of phase responses in cKPFM measurements under illumination. Individual cKPFM curves at the 'x' marked in (g) yellow, (h) green, (i) purple, and (j) lightblue in (f). The 1st PCA component of mean deviation from cKPFM data (k) in the dark and (l) under illumination.

inhomogeneity or differences in local crystallographic orientations. These properties can contribute to a localized ferroelectric or non-ferroelectric nature in 2D MHPs. Under illumination, such dependence disappears due to the absence of ferroelectric behavior. This local polarization is frequently observed in classical oxides51 and originates from the inhomogeneity of surface defects. Thus, the observed local ferroelectricity can be due to several reasons such as chemical

inhomogeneity, variation in preferential crystallographic orientation, presence of defects, and their redistribution.

To further analyze the cKPFM data and separate the noise signals from the complex coupled responses in the original data, principal component analysis (PCA) from the mean deviation of cKPFM data is performed on both spectroscopy maps in the dark and under illumination. We choose the PCA approach as it is one of the classical dimensionality reduction techniques with a relatively low computational cost for large datasets. Our recent study provides a detailed explanation of the PCA approach in cKPFM data. From the PCA analysis, the 4D cKPFM data ( $V_{\rm read}$ ,  $V_{\rm write}$ , x, y) can be deconvoluted to a 3D data set  $R_{\rm av}$  ( $V_{\rm read}$ , x, y) where  $R_{\rm av}$  represents the average responses. The cKPFM data set is analyzed by PCA as below:

PCA space 
$$(R^k) = \sum_{i=1}^N R^M(x_i - \mu)$$

where  $R^{\rm M}$ ,  $x_i$ , and  $\mu$  represent the original space, centering data, and mean. To preserve the original data, we have selected the most k eigenvectors, e.g.  $\{V_1, ..., V_k\}$  in the PCA space. Here, the number of the optimized components (eigenvectors) is three. Fig. 3k and I show the loading maps of the 1st PCA component in the dark and under illumination. The loading maps show the spatial distribution of the averaged responses in the cKPFM data set. The eigenvectors  $(R_{av})$  for the 1<sup>st</sup> component as a function of  $V_{\rm read}$  are presented in Fig. S11.† These are the same trends for  $R_{\rm av}$  under both conditions, which is related to a pure electrostatic response. The 2<sup>nd</sup> and 3<sup>rd</sup> components are displayed in Fig. S12.† The loading map in the 2<sup>nd</sup> component (Fig. S12a†) also shows red color regions with a downward trend of the  $R_{\rm av}$  response. However, there are noise responses in the  $3^{\rm rd}$  component since  $R_{\rm av}$  is not straightforward. As the  $3^{\rm rd}$ component is not meaningful due to the noise response, we only consider the 1st and 2nd components that are related to the pure electrostatic response from the PCA approach. Nonetheless, the red color regions in the 1st component (Fig. 3k) are well-matched with hysteretic behaviors as analyzed in the original data. The red color regions are remarkably clustered in the dark while these regions can be seen rarely under illumination (Fig. 31). These non-contrast responses are the same in the 2<sup>nd</sup> component (see Fig. S12c†). This phenomenon is unique as typically light drives the enhanced ferroelectric polarization in classical ferroelectrics. 52,53 Hence, it is necessary to further study the origin of the light-ferroelectricity interactions in this material.

It is known that in MHPs, the photogenerated charge carriers under illumination can contribute to the higher density of charge carriers. Thus, such a smaller band dispersion can be associated with the absence of ferroelectricity under illumination rather than a simply reduced density of charge carriers. The weakened ferroelectricity can be possibly due to a change of preferential crystallographic directions and organic cation decomposition which is explored in the following section. Another possible scenario is that if higher band dispersion in the cKPFM response originates from the interplay between

injected charge carriers and intrinsic defects, *e.g.*, trapped/detrapped charge carriers, under dark conditions, excess photogenerated charge carriers can fill the traps, which leads to reduction of band dispersion due to the decrease of defect densities. This will be explored in our future studies. However, the ferroelectricity has been revealed in the 2D MHPs, thus lowering band dispersion is significantly responsible for the weak ferroelectricity response under illumination.

To explore the origin of light–ferroelectricity interaction, we perform *in situ* XRD measurements under illumination and upon application of electric bias. The biases are applied vertically to a planar device structure to provide similar experimental conditions to the cKPFM measurements, which are described in Fig. S13.† For this measurement, we deposited a thin layer of Au electrode (around 50 nm) on top of the perovskite film surface. Note that the source bias is connected to the bottom ITO electrode. During our measurements, there is no major damage to the film structure as shown by new diffraction peaks such as PbI<sub>2</sub> near 15° as evidence for degradation of the film.<sup>54</sup> Besides, we cannot find any remarkable changes in the peaks related to Au and ITO as marked with stars and hashes, respectively.

Fig. 4a-c show the stacked XRD patterns under light and bias conditions. The extent of crystallinity on individual planes is variable depending on the electrical bias as well as under illumination. First, it is evident that some planes, especially the peaks below 25° are influenced by illumination as shown in Fig. 4a. The enlarged XRD peaks in Fig. 4a are presented in Fig. S14.† Particularly, as shown in Fig. S14a,† the peak intensity of the (0 2 0) plane decreases under illumination, and then it is partially back to the pristine condition when the sample is back to dark conditions. However, the intensity of the (1 1 1) plane (Fig. S14b†) does not return to the original condition after the intensity decreases by illumination. In addition, the intensity of the (0 6 0) plane (Fig. S14c†) under illumination is further decreased when the sample is back to dark conditions. We note that the rest of the planes beyond 25°  $2\theta$  do not change during the experiment (Fig. S14d†). The changes in the XRD peak intensities can be associated with structural changes. Our previous study demonstrated light-induced structural variations measured by peak broadening from in situ XRD measurements in 3D MHPs.35 However, we cannot observe the pronounced peak broadening in the XRD results of 2D MHPs due to their more stable structure, which could be attributed to the variation in the degree of crystallinity. It should be noted that the higher light intensity may change the structure. Here, we use an LED light source with an intensity of  $\sim 5$  mW cm<sup>-2</sup>. Next, we explore the effect of electrical bias on crystallinity of the 2D perovskite sample. Fig. 4b shows the stacked XRD patterns when positive and negative biases of  $\pm 10$  V are applied to the sample in the dark. Interestingly, a significant increase in the intensities of the XRD peaks is observed, in particular, for the (0 2 0), (1 1 1), and (0 6 0) planes once +10 V is applied to the sample (see Fig. S15a-c†). The increased intensity remains constant during the application of -10 V. Despite the removal of biases, the change in the intensities of peaks is not reversible. Similarly, the rest of the peaks beyond  $25^{\circ}$   $2\theta$  (Fig. S15d†) remain constant during our measurements. Then, we perform

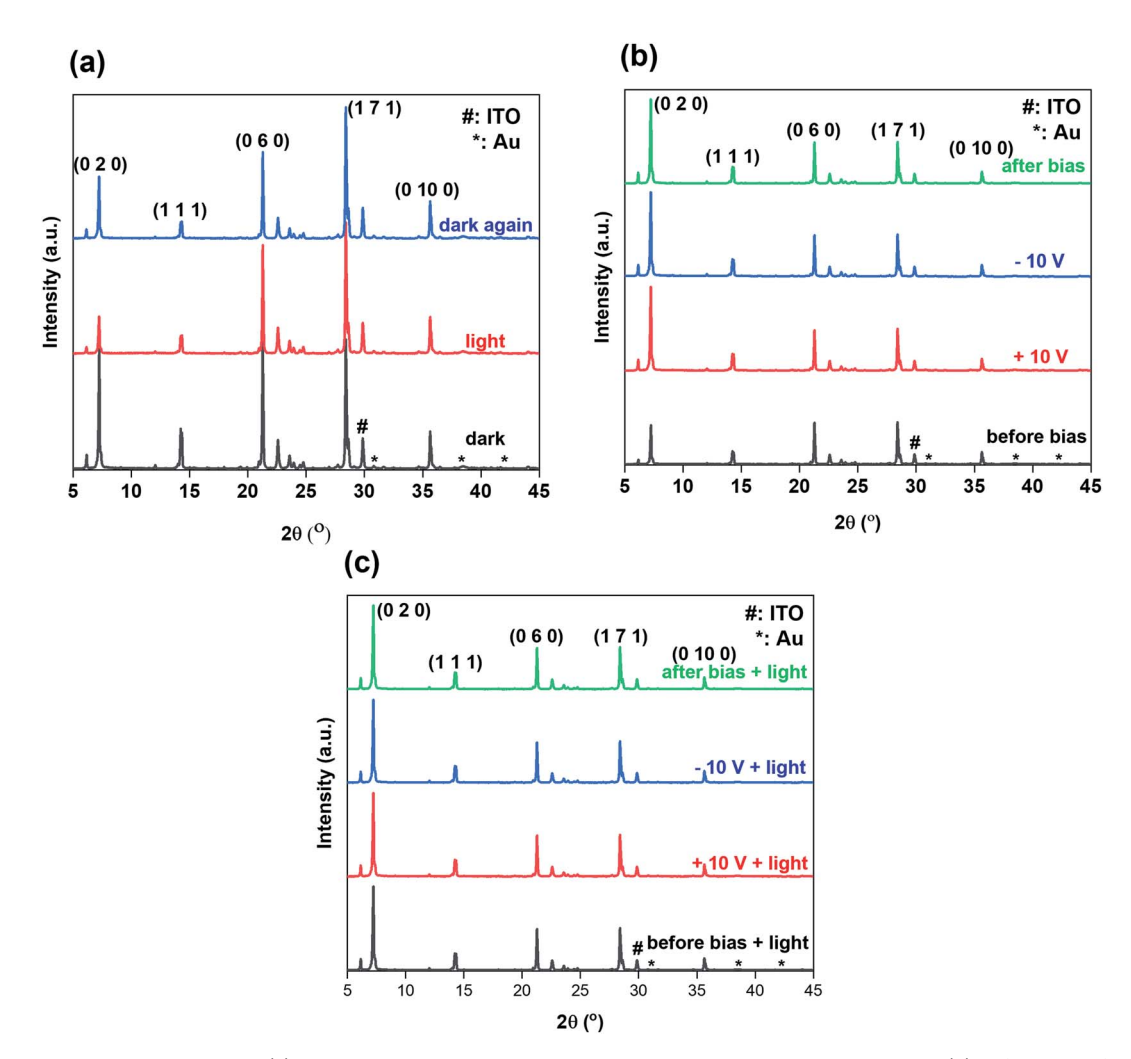


Fig. 4 The in situ XRD measurements. (a) The stacked XRD patterns under dark-illumination-dark conditions, (b) before and after biasing with +10 V, -10 V, and back to no bias in the dark, (c) before and after biasing with +10 V and -10 V under illumination and back to the pristine (no bias; dark conditions).

XRD measurements by applying electrical biases under illumination as shown in Fig. 4c. However, we do not observe any noticeable changes in the XRD peaks. Continuous application of bias results in an irreversible effect on the crystallinity (see Fig. 4c). Note that the electric field in this measurement is much stronger as compared to the application of FORC bias (on- and off-fields with a 16 millisecond duration) for the cKPFM measurements. Nonetheless, from our XRD studies, it is observed that the (0 2 0), (1 1 1), (0 6 0) lattice planes are more sensitive to the light-induced crystallinity change. For the 2D perovskite crystals, a crystallographic direction along [001] is associated with the ferroelectric phase due to the perpendicular polarization direction between quantum wells while the [110] directions lead to the paraelectric phase.17 Hence, growth of the (0 2 0) plane can annihilate the ferroelectric behavior rather than that of the (1 1 1) plane in our result (Fig. 4a). This crystallographic orientation-modulated ferroelectricity is previously observed in classical ferroelectrics. 55-57 It can be argued that the significant growth of the horizontal plane induced by

illumination and electrical biases contributes to the removal of ferroelectricity in this material.

To further elucidate the origin of light-ferroelectricity interaction, we perform ToF-SIMS on 2D perovskite films in the dark and under illumination. The mass spectra of positive and negative ions are shown in Fig. 5. As can be seen in the spectra of positive ions (Fig. 5a), the DFPD<sup>+</sup> ion concentration distinctly decreases under illumination as compared to dark conditions, while the concentration of other positive ions is not changed. The corresponding chemical maps of these ions are shown in Fig. S16.† The pronounced decrease in the concentration of DFPD<sup>+</sup> ion under illumination is possibly responsible for the weakening or vanishing ferroelectricity as observed in cKPFM measurements. This is because organic cations play an important role in determining ferroelectricity in 2D MHPs. When returning to dark conditions, additional decreases in the concentration of other positive ions (MA+ and other organic products) as well as the DFPD<sup>+</sup> ion are observed. An unknown organic component is detected at a mass between 80 and 100, marked with a star in Fig. 5a, which possibly originates from the

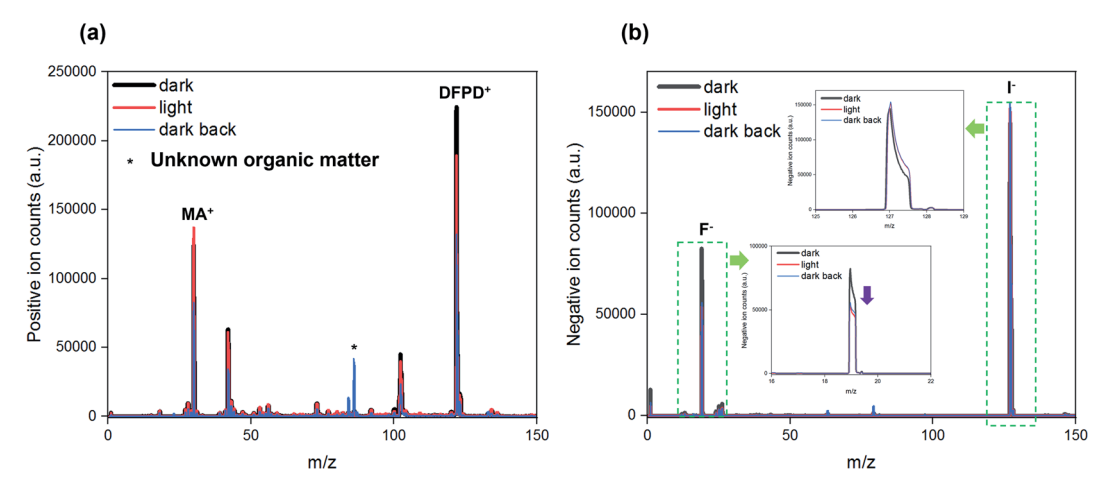


Fig. 5 Time of flight secondary ion mass spectrometry (ToF-SIMS) spectra of (a) positive ions and (b) negative ions under dark-illumination-dark conditions. The mainly contributed components represent DFPD<sup>+</sup> and MA<sup>+</sup> ions in the mass spectra of positive ions, and the major peaks are I<sup>-</sup> and F<sup>-</sup> in the mass spectra of negative ions.

decomposition of organic component under illumination. Recently, we observed organic component decomposition using time-resolved ToF-SIMS in MAPbI3 thin films in a lateral electrode device which is attributed to the bias-induced decomposition of the MA<sup>+</sup> organic cation.<sup>58</sup> In this study,<sup>58</sup> the mass spectra of positive ions showed several peaks that are associated with the byproducts of MA<sup>+</sup> decomposition appearing at masses between 40 and 80. Thus, the unknown organic component could be responsible for the decomposition of the DFPD<sup>+</sup> cation. This result indicates that the change in the organic cation chemistry can result in the weakening of ferroelectricity and the loss of dipole moment.

As can be seen in the mass spectra of negative ions (Fig. 5b), we observe relatively stable I ion dynamics in the dark and under illumination, while the concentration of F ions decreases significantly under illumination, and this change is not recoverable. The corresponding chemical maps are displayed in Fig. S17.† We speculate that this phenomenon results from the decomposition of the DFPD component (containing F ions) as observed in positive ion dynamics. Interestingly, we observe a depleted region in larger scan areas (100 μm<sup>2</sup>) in the F ion map after the above ToF-SIMS measurements (see Fig. S18†). These results further confirm unstable chemical dynamics in (4,4-DFPD)<sub>2</sub>PbI<sub>4</sub> perovskites under illumination which leads to light-induced ferroelectricity modulation.

Compared to 3D (ABX<sub>3</sub>) MHPs, there is a wide variety of candidates for the A-site cation in 2D (A2BX4) MHPs with longer organic chains, leading to enhanced stability under ambient conditions due to the hydrophobicity of the long-chain cations. However, considering the molecular structure, structural difference, and polarization, different ferroelectricity behaviors in the distinct MHP structure and composition can be speculated. For instance, the size of the A-site cation in 3D MHPs is limited to around 2.6 Å by Goldschmidt geometry rules.<sup>59</sup> In comparison, for 2D MHPs, not only the size of the cation is relatively larger but also the separated layer (quantum wells) thickness by the cation is larger over 10 Å. The unique larger A-

site cation and structure in 2D MHPs provide additional asymmetry, which results in ferroelectricity classified as the order-disorder type. While 3D MHPs show relatively lower ferroelectric responses that originate from the displacement of a smaller A-site cation called a displacive type. The difference of these molecular structures thus leads to different rotational properties of the polar cations in 3D and 2D MHPs. Therefore, significantly different ferroelectric dynamics can be expected in two different classes of MHPs.

As discussed, in 2D MHPs, the organic cation motions are responsible for ferroelectricity. Particularly, multiple quantum wells where organic cations are placed between inorganic layers lead to higher ferroelectricity in 2D MHPs. In our study, the observed phenomenon can be dependent on the stability of organic cations under illumination and biasing conditions. Here, tunning preferential crystallographic directions can result in the vanishing of ferroelectricity. In fact, spontaneous polarization which is an indication of ferroelectricity is very different in a variety of organic cations as well as halide ions.9

We have explored ferroelectricity and the origin of lightferroelectricity interaction using BE-PFM, cKPFM, in situ XRD, and ToF-SIMS measurements. In the dark, ferroelectricity is confirmed by hysteretic behaviors in cKPFM responses. Under illumination, the observed ferroelectricity experiences a transition to the paraelectric phase. In MHPs, organic molecule cations play a critical role in determining the polarization where their orientation causes local potential fluctuations leading to highly orientated ferroelectric domain structures and domain walls.60-62 These localized features improve charge carrier transport by reducing carrier recombination<sup>63</sup> as the existence of ferroelectric domains prevents scattering of charge carriers. 64 Although a light-driven giant dielectric constant was observed in 3D MHPs, 33,65 weakening ferroelectricity under illumination is a unique characteristic in 2D MHPs. Previously, light-induced polarization reordering has been proposed as the origin of the improved ferroelectricity under illumination in 3D MHPs.66,67 This phenomenon was explained by reordering of the dipole moments of organic cation under illumination, resulting from variation in crystallographic orientation.68 For example, the [110] direction that is composed of head-to-head and tail-to-tail components where the head-to-head component presents the same polarization direction and the tail-to-tail component represents the opposite polarization direction leads to stronger one-dimensional potential wells, thus creating higher ferroelectricity.68 In contrast, 2D MHP contains layer-by-layer potential wells where the perpendicular direction [001] to the layer is associated with ferroelectricity. This structural characteristic has led to higher ferroelectricity in 2D MHPs rather than in 3D MHP.9 However, based on our results, light-driven preferential orientation modulation, e.g. decreased intensity of (1 1 1) lattice planes can lead to the weakening of ferroelectricity, possibly resulting from minor structural variations. Further, the instability of organic cations due to ion migration or volatility under illumination could result in degradation leading to the disappearance of ferroelectricity. Note that the ion migration under illumination can also screen ferroelectric polarization.46 This study elucidates the origin of ferroelectric instability in (4,4-DFPD)<sub>2</sub>PbI<sub>4</sub> thin films, which is important for clarifying light-ferroelectric interaction in 2D MHPs.

# Conclusions

In summary, the BE-PFM measurements demonstrate ferroelectric domain structures on the (4,4-DFPD)<sub>2</sub>PbI<sub>4</sub> 2D film surface in the dark and under illumination. The c-KPFM responses reveal hysteretic cKPFM loops in the dark. The hysteretic dynamics are highly dependent on domain structures in the dark. However, hysteresis is dramatically reduced in similar regions under illumination. The XRD results under illumination provide information on crystallographic orientation change. Specifically, the intensities on both (0 2 0) and (1 1 1) lattice planes are decreased under illumination. The reduction in the intensity of the (1 1 1) plane that is associated with the ferroelectric phase in this material can contribute to the transition from ferroelectricity to paraelectricity under illumination. Further, the chemical analysis using ToF-SIMS reveals that the positive organic cation and the corresponding negative F ion are unstable under illumination while the concentration of I<sup>-</sup> negative ion remains constant during the measurements. Consequently, both crystallinity and chemical dynamics can have an influence on ferroelectric properties in (4,4-DFPD)<sub>2</sub>PbI<sub>4</sub> thin films. These results highlight that the light-ferroelectricity interaction originates from crystallographic orientations and chemical composition instability in 2D MHPs. We stress that crystallography and chemical engineering is the key element for more stable ferroelectricity in 2D MHPs.

# **Experimental section**

#### Single crystal growth

(4,4-Difluoropiperidinium)<sub>2</sub>PbI<sub>4</sub> single crystals were grown by slow cooling crystallization. 4,4-Difluoropiperidinium hydrochloride (DFPD, 0.1 M, Sigma-Aldrich) is dissolved in the HI solution (10 mL, 57 wt% in H2O, Sigma-Aldrich) and then

stirred at room temperature for 1 h. Then PbI2 (0.05 M, Sigma-Aldrich) is added to the solution. An orange powder precipitates from the undissolved PbI2 which was dissolved by heating the solution to 405 K in an oil bath. The solution was kept at the same temperature for 1 h, forming a clear solution. Slowly cooling the solution to room temperature for around 14 days produced needle shape crystals of (4,4-DFPD)<sub>2</sub>PbI<sub>4</sub>.

#### Thin film fabrication

The as-grown (4,4-DFPD)<sub>2</sub>PbI<sub>4</sub> crystals (60 mg) are dissolved in dimethyl sulfoxide (DMSO, 200 µL) to prepare the precursor solution. The ITO (indium tin oxide)-coated glass substrates (MSE Pro<sup>TM</sup>,  $15 \times 15 \times 1$  mm<sup>3</sup>) were precleaned using deionized water, acetone, and isopropanol in an ultrasonic bath for 15 min, respectively. After the initial cleaning, the glass substrates were treated under UV ozone for 15 min. Then, the substrates were transferred into an N2-filled glove box. For dropcasting, a precleaned ITO glass was placed on a hotplate at 373 K, and then about 5 μL of the precursor solution was carefully dropped on the hot substrate and dried for 10 min for full crystallization.

#### Characterization and data analysis

Scanning Probe Microscopy (SPM) measurements: AFM, **PFM**, **BE-PFM**, and **cKPFM**. The thin films were characterized by atomic force microscopy (AFM, MFP-3D, Asylum Research) under ambient conditions at room temperature. All SPM measurements were performed using a Pt/Ir coated Si cantilever (ElectriMulti 75-G, Budget Sensors). For piezo-response force microscopy (PFM), an AC drive amplitude (3 V) was applied to the PFM tip to achieve a sharp contact resonance peak. All PFM data were obtained with the out-of-plane amplitude and phase in the same scan. For illumination, white LED sources that are not filtered illuminate the sample from the bottom area through the glass substrate. In all PFM measurements, the scan rate is fixed at 1.0 Hz, and the scan direction starts from top to the bottom.

Band-excitation piezo-response force microscopy (BE-PFM) and contact Kelvin probe force microscopy (cKPFM) measurements. Band excitation (BE)-PFM and contact Kelvin probe force microscopy (cKPFM) were carried out using an AFM (MFP-3D, Asylum Research) with an in-house controller (Look Instrument) and Labview-based software. The same AFM tip was used as above. The BE mode uses a digitally synthesized AC voltage across a range of frequencies. A built-in lock-in amplifier was used to enhance the signal-to-noise ratio in all BE-PFM and cKPFM measurements. The frequency range in the BE measurements was centered at 380 kHz with a bandwidth of 100 kHz, and the drive amplitude for BE-PFM excitation was 3 V. The BE-PFM measurements were taken over a grid of  $256 \times 256$ points on the sample surface. BE-PFM responses such as the amplitude, phase, frequency, and Q-factor are obtained using a simple harmonic oscillator (SHO) model. The cKPFM measurements were taken over a grid of 40 by 40 points on the film surface. For the cKPFM measurements, a DC write voltage was applied stepwise from 0, +10 V, 0 V, -10 V, and back to zero consecutively with totally 32 steps. These applied voltage steps are referred to as  $V_{\rm write}$ . Between all  $V_{\rm write}$  steps, there is a read bias step ( $V_{\rm read}$ ), where the piezo-response and cKPFM response are measured with totally 7 steps between -10 and +10 V. The delay time between subsequent measurements is in milliseconds. The piezo-response measured at 0 V during the read measurements is shown in the off-field response. Likewise, the sample was illuminated from the white LED source sources located at the bottom area.

Principle component analysis (PCA) of cKPFM data. The 4D cKPFM data set can be well represented as a bimodal 3D data set  $R_{\rm av}$  ( $V_{\rm read}$ , x, y) and  $R_{\rm delta}$  ( $V_{\rm read}$ , x, y).  $R_{\rm av}$  represents the average  $V_{\rm read}$ , and  $R_{\rm delta}$  represents the corresponding dispersion. PCA is performed using pycroscopy based on universal spectroscopy and the imaging data model on a Jupyter Notebook for Python 3. To gain PCA components and the corresponding loading maps from the mean deviation of the cKPFM data, these are computed using Scikit-Learn's PCA estimator.

X-Ray Diffraction (XRD) measurements. The crystal structure and crystal orientation of the films were characterized by using a high-resolution X-ray diffractometer (X'Pert Pro, Panalytical). The X-ray diffractometer uses Cu K $\alpha$  radiation.

Time-of-Flight-Secondary Ion Mass Spectrometry (ToF-SIMS) measurements. ToF-SIMS measurements were performed using a ToF.SIMS-5-NCS instrument (IONTOF GmbH, Germany). The experiments were carried out in both negative and positive ion modes with spectra calibrated using the  $I^-$ ,  $F^-$ ,  $C_5H_9F_2N^+$  and  $Pb^+$  peaks. A built-in LED white light in the ToF-SIMS chamber is used for illumination.

## Author contributions

Dohyung Kim: conceptualization, investigation, validation, resources, data curation, visualization, and writing – original draft. Anton V. Ievlev: investigation, data curation, visualization, and writing – review & draft. Olga S. Ovchinnikova: resources and writing – review & draft. Sergei V. Kalinin: conceptualization and writing – review & draft. Mahshid Ahmadi: conceptualization, supervision, project administration, funding acquisition, and writing – review & draft.

## Conflicts of interest

There are no conflicts to declare.

# Acknowledgements

M. A. acknowledges support from the National Science Foundation (NSF), Award Number # 2043205. D. K. and M. A. acknowledge support from the University of Tennessee and CNMS user facility, project # CNMS2021-A-00706. The ToF-SIMS measurements were conducted and supported (A. V. I, O. S. O, S. V. K.) by the Center for Nanophase Materials Science (CNMS), which is a DOE Office of Science User Facility. O. S. O. was supported through the DOE Office of Science Research Program for Microelectronics Codesign (sponsored by ASCR, BES, HEP,

NP, and FES) through the Abisko Project, PM Robinson Pino (ASCR). S. V. K. acknowledges the support of the 3DFeM EFRC center. XRD was performed at the Institute for Advanced Materials and Manufacturing (IAMM) Diffraction Facility, located at the University of Tennessee, Knoxville.

## References

- 1 W. Li, Z. Wang, F. Deschler, S. Gao, R. H. Friend and A. K. Cheetham, *Nat. Rev. Mater.*, 2017, 2, 16099.
- 2 G. Long, R. Sabatini, M. I. Saidaminov, G. Lakhwani, A. Rasmita, X. Liu, E. H. Sargent and W. Gao, *Nat. Rev. Mater.*, 2020, 5, 423–439.
- 3 Y. Fu, H. Zhu, J. Chen, M. P. Hautzinger, X. Y. Zhu and S. Jin, *Nat. Rev. Mater.*, 2019, 4, 169–188.
- 4 G. Grancini and M. K. Nazeeruddin, *Nat. Rev. Mater.*, 2019, 4, 4–22.
- 5 I. C. Smith, E. T. Hoke, D. Solis-Ibarra, M. D. McGehee and H. I. Karunadasa, *Angew. Chem., Int. Ed.*, 2014, 53, 11232– 11235.
- 6 F. O. Saouma, C. C. Stoumpos, J. Wong, M. G. Kanatzidis and J. I. Jang, *Nat. Commun.*, 2017, 8, 742.
- 7 R. Zhuang, X. Wang, W. Ma, Y. Wu, X. Chen, L. Tang, H. Zhu, J. Liu, L. Wu, W. Zhou, X. Liu and Y. Yang, *Nat. Photonics*, 2019, 13, 602–608.
- 8 M. Seitz, A. J. Magdaleno, N. Alcázar-Cano, M. Meléndez, T. J. Lubbers, S. W. Walraven, S. Pakdel, E. Prada, R. Delgado-Buscalioni and F. Prins, *Nat. Commun.*, 2020, 11, 2035.
- 9 Y. Hou, C. Wu, D. Yang, T. Ye, V. G. Honavar, A. C. T. van Duin, K. Wang and S. Priya, *J. Appl. Phys.*, 2020, **128**, 060906.
- 10 J. F. Scott, Science, 2007, 315, 954.
- W.-Q. Liao, Y. Zhang, C.-L. Hu, J.-G. Mao, H.-Y. Ye, P.-F. Li,
   S. D. Huang and R.-G. Xiong, *Nat. Commun.*, 2015, 6, 7338.
- 12 H.-Y. Ye, W.-Q. Liao, C.-L. Hu, Y. Zhang, Y.-M. You, J.-G. Mao, P.-F. Li and R.-G. Xiong, *Adv. Mater.*, 2016, **28**, 2579–2586.
- 13 C. Ji, S. Wang, L. Li, Z. Sun, M. Hong and J. Luo, *Adv. Funct. Mater.*, 2019, **29**, 1805038.
- 14 C.-K. Yang, W.-N. Chen, Y.-T. Ding, J. Wang, Y. Rao, W.-Q. Liao, Y.-Y. Tang, P.-F. Li, Z.-X. Wang and R.-G. Xiong, Adv. Mater., 2019, 31, 1808088.
- 15 P.-P. Shi, S.-Q. Lu, X.-J. Song, X.-G. Chen, W.-Q. Liao, P.-F. Li, Y.-Y. Tang and R.-G. Xiong, J. Am. Chem. Soc., 2019, 141, 18334–18340.
- 16 H. Fu, C. Jiang, J. Lao, C. Luo, H. Lin, H. Peng and C.-G. Duan, CrystEngComm, 2020, 22, 1436–1441.
- 17 H.-Y. Zhang, X.-J. Song, X.-G. Chen, Z.-X. Zhang, Y.-M. You, Y.-Y. Tang and R.-G. Xiong, J. Am. Chem. Soc., 2020, 142, 4925–4931.
- 18 X.-G. Chen, X.-J. Song, Z.-X. Zhang, H.-Y. Zhang, Q. Pan, J. Yao, Y.-M. You and R.-G. Xiong, J. Am. Chem. Soc., 2020, 142, 10212–10218.
- 19 X.-G. Chen, X.-J. Song, Z.-X. Zhang, P.-F. Li, J.-Z. Ge, Y.-Y. Tang, J.-X. Gao, W.-Y. Zhang, D.-W. Fu, Y.-M. You and R.-G. Xiong, *J. Am. Chem. Soc.*, 2020, 142, 1077–1082.
- 20 H.-Y. Liu, H.-Y. Zhang, X.-G. Chen and R.-G. Xiong, *J. Am. Chem. Soc.*, 2020, **142**, 15205–15218.

- 21 H.-Y. Zhang, Y.-Y. Tang, P.-P. Shi and R.-G. Xiong, *Acc. Chem. Res.*, 2019, **52**, 1928–1938.
- 22 Y.-Y. Tang, Y. Xie, Y.-L. Zeng, J.-C. Liu, W.-H. He, X.-Q. Huang and R.-G. Xiong, *Adv. Mater.*, 2020, **32**, 2003530.
- 23 Z.-X. Wang, Y. Zhang, Y.-Y. Tang, P.-F. Li and R.-G. Xiong, J. Am. Chem. Soc., 2019, 141, 4372–4378.
- 24 D. Kim, B. Dryzhakov, Y. Liu, O. S. Ovchinnikova, B. Hu, S. V. Kalinin and M. Ahmadi, *Chem. Mater.*, 2021, 33, 4077–4088.
- 25 R. Pandey, G. Vats, J. Yun, C. R. Bowen, A. W. Y. Ho-Baillie, J. Seidel, K. T. Butler and S. I. Seok, *Adv. Mater.*, 2019, 31, 1807376.
- 26 A. N. Morozovska, E. A. Eliseev, N. V. Morozovsky and S. V. Kalinin, *Phys. Rev. B*, 2017, **95**, 195413.
- 27 Y. Liu, D. Kim, A. V. Ievlev, S. V. Kalinin, M. Ahmadi and O. S. Ovchinnikova, Adv. Funct. Mater., 2021, 2102793.
- 28 Y.-T. Li, L. Ding, J.-Z. Li, J. Kang, D.-H. Li, L. Ren, Z.-Y. Ju, M.-X. Sun, J.-Q. Ma, Y. Tian, G.-Y. Gou, D. Xie, H. Tian, Y. Yang, L.-W. Wang, L.-M. Peng and T.-L. Ren, ACS Cent. Sci., 2019, 5, 1857–1865.
- 29 S. Jariwala, H. Sun, G. W. P. Adhyaksa, A. Lof, L. A. Muscarella, B. Ehrler, E. C. Garnett and D. S. Ginger, *Joule*, 2019, 3, 3048–3060.
- 30 S. Y. Leblebici, L. Leppert, Y. Li, S. E. Reyes-Lillo, S. Wickenburg, E. Wong, J. Lee, M. Melli, D. Ziegler, D. K. Angell, D. F. Ogletree, P. D. Ashby, F. M. Toma, J. B. Neaton, I. D. Sharp and A. Weber-Bargioni, *Nat. Energy*, 2016, 1, 16093.
- 31 D. Kim, J.-H. Yun, M. Lyu, J. Kim, S. Lim, J. S. Yun, L. Wang and J. Seidel, *J. Phys. Chem. C*, 2019, **123**, 14144–14151.
- 32 Y. Liu, P. Trimby, L. Collins, M. Ahmadi, A. Winkelmann, R. Proksch and O. S. Ovchinnikova, *ACS Nano*, 2021, **15**, 7139–7148.
- 33 E. J. Juarez-Perez, R. S. Sanchez, L. Badia, G. Garcia-Belmonte, Y. S. Kang, I. Mora-Sero and J. Bisquert, *J. Phys. Chem. Lett.*, 2014, 5, 2390–2394.
- 34 M. Coll, A. Gomez, E. Mas-Marza, O. Almora, G. Garcia-Belmonte, M. Campoy-Quiles and J. Bisquert, *J. Phys. Chem. Lett.*, 2015, **6**, 1408–1413.
- 35 D. Kim, J. S. Yun, P. Sharma, D. S. Lee, J. Kim, A. M. Soufiani, S. Huang, M. A. Green, A. W. Y. Ho-Baillie and J. Seidel, *Nat. Commun.*, 2019, 10, 444.
- 36 R. K. Vasudevan, N. Balke, P. Maksymovych, S. Jesse and S. V. Kalinin, *Appl. Phys. Rev.*, 2017, 4, 021302.
- 37 N. Balke, P. Maksymovych, S. Jesse, A. Herklotz, A. Tselev, C.-B. Eom, I. I. Kravchenko, P. Yu and S. V. Kalinin, *ACS Nano*, 2015, **9**, 6484–6492.
- 38 Y. Liu, N. Borodinov, M. Lorenz, M. Ahmadi, S. V. Kalinin, A. V. Ievlev and O. S. Ovchinnikova, *Adv. Sci.*, 2020, 7, 2001176.
- 39 M. Ahmadi, L. Collins, K. Higgins, D. Kim, E. Lukosi and S. V. Kalinin, ACS Appl. Mater. Interfaces, 2019, 11, 41551– 41560
- 40 D. Kim, E. S. Muckley, N. Creange, T. H. Wan, M. H. Ann, E. Quattrocchi, R. K. Vasudevan, J. H. Kim, F. Ciucci, I. N. Ivanov, S. V. Kalinin and M. Ahmadi, *Adv. Sci.*, 2021, 8, 2002510.

- 41 D. Kim, Y. Liu, A. V. Ievlev, K. Higgins, O. S. Ovchinnikova, J. S. Yun, J. Seidel, S. V. Kalinin and M. Ahmadi, *Nano Energy*, 2021, 89, 106428.
- 42 J. S. Yun, J. Seidel, J. Kim, A. M. Soufiani, S. Huang, J. Lau, N. J. Jeon, S. I. Seok, M. A. Green and A. Ho-Baillie, Adv. Energy Mater., 2016, 6, 1600330.
- 43 M. H. Futscher, J. M. Lee, L. McGovern, L. A. Muscarella, T. Wang, M. I. Haider, A. Fakharuddin, L. Schmidt-Mende and B. Ehrler, *Mater. Horiz.*, 2019, **6**, 1497–1503.
- 44 Y. Lin, Y. Bai, Y. Fang, Q. Wang, Y. Deng and J. Huang, *ACS Energy Lett.*, 2017, **2**, 1571–1572.
- 45 D. Kim, R. K. Vasudevan, K. Higgins, A. Morozovska, E. A. Eliseev, M. Ziatdinov, S. V. Kalinin and M. Ahmadi, J. Phys. Chem. C, 2021, 125, 12355–12365.
- 46 M. Ahmadi, L. Collins, A. Puretzky, J. Zhang, J. K. Keum, W. Lu, I. Ivanov, S. V. Kalinin and B. Hu, *Adv. Mater.*, 2018, 30, 1705298.
- 47 A. Gruverman, M. Alexe and D. Meier, *Nat. Commun.*, 2019, **10**, 1661.
- 48 N. Balke, P. Maksymovych, S. Jesse, I. I. Kravchenko, Q. Li and S. V. Kalinin, *ACS Nano*, 2014, **8**, 10229–10236.
- 49 D. Kim, R. K. Vasudevan, K. Higgins, A. Morozovska, E. A. Eliseev, M. Ziatdinov, S. V. Kalinin and M. Ahmadi, J. Phys. Chem. C, 2021, 125, 12355–12365.
- 50 S. M. Yang, A. N. Morozovska, R. Kumar, E. A. Eliseev, Y. Cao, L. Mazet, N. Balke, S. Jesse, R. K. Vasudevan, C. Dubourdieu and S. V. Kalinin, *Nat. Phys.*, 2017, 13, 812–818.
- 51 S. V. Kalinin, A. N. Morozovska, L. Q. Chen and B. J. Rodriguez, *Rep. Prog. Phys.*, 2010, 73, 056502.
- 52 H. Borkar, V. Rao, M. Tomar, V. Gupta, J. F. Scott and A. Kumar, *Mater. Today Commun.*, 2018, 14, 116–123.
- 53 H. Borkar and A. Kumar, Vacuum, 2018, 153, 91-95.
- 54 Y. Yuan, Q. Wang, Y. Shao, H. Lu, T. Li, A. Gruverman and J. Huang, *Adv. Energy Mater.*, 2016, **6**, 1501803.
- 55 N.-K. Kim, S.-J. Yeom, S.-Y. Kweon, E.-S. Choi, H.-J. Sun, H.-C. Sohn and J.-S. Roh, *Integr. Ferroelectr.*, 2005, **70**, 89–97.
- 56 R. Ding, D. Wang, D. Chu and S. Li, *J. Am. Ceram. Soc.*, 2013, **96**, 3530–3535.
- 57 R. Ramesh, T. Sands and V. G. Keramidas, *Appl. Phys. Lett.*, 1993, **63**, 731–733.
- 58 Y. Liu, N. Borodinov, L. Collins, M. Ahmadi, S. V. Kalinin, O. S. Ovchinnikova and A. V. Ievlev, ACS Nano, 2021, 15, 9017–9026.
- 59 J.-P. Correa-Baena, M. Saliba, T. Buonassisi, M. Grätzel, A. Abate, W. Tress and A. Hagfeldt, *Science*, 2017, 358, 739–744.
- 60 J. M. Frost, K. T. Butler, F. Brivio, C. H. Hendon, M. van Schilfgaarde and A. Walsh, *Nano Lett.*, 2014, 14, 2584–2590.
- 61 J. M. Frost, K. T. Butler and A. Walsh, APL Mater., 2014, 2, 081506.
- 62 S. Liu, F. Zheng, N. Z. Koocher, H. Takenaka, F. Wang and A. M. Rappe, J. Phys. Chem. Lett., 2015, 6, 693–699.
- 63 A. Pecchia, D. Gentilini, D. Rossi, M. Auf der Maur and A. Di Carlo, *Nano Lett.*, 2016, **16**, 988–992.
- 64 K. Miyata and X. Y. Zhu, Nat. Mater., 2018, 17, 379-381.
- 65 I. Anusca, S. Balčiūnas, P. Gemeiner, Š. Svirskas, M. Sanlialp, G. Lackner, C. Fettkenhauer, J. Belovickis, V. Samulionis,

- M. Ivanov, B. Dkhil, J. Banys, V. V. Shvartsman and D. C. Lupascu, *Adv. Energy Mater.*, 2017, 7, 1700600.
- 66 T. Wu, L. Collins, J. Zhang, P.-Y. Lin, M. Ahmadi, S. Jesse and B. Hu, *ACS Nano*, 2017, **11**, 11542–11549.
- 67 P. Wang, J. Zhao, L. Wei, Q. Zhu, S. Xie, J. Liu, X. Meng and J. Li, *Nanoscale*, 2017, **9**, 3806–3817.
- 68 H.-C. Hsu, B.-C. Huang, S.-C. Chin, C.-R. Hsing, D.-L. Nguyen, M. Schnedler, R. Sankar, R. E. Dunin-Borkowski, C.-M. Wei, C.-W. Chen, P. Ebert and Y.-P. Chiu, *ACS Nano*, 2019, **13**, 4402–4409.